








Constraints on the properties of ν MSM dark matter using the satellite galaxies of the Milky Way

Oliver Newton ¹* Mark R. Lovell ² Carlos S. Frenk ² Adrian Jenkins ² John C. Helly ²
Shaun Cole ² and Andrew J. Benson ³

¹Center for Theoretical Physics, Polish Academy of Sciences, al. Lotników 32/46 Warsaw, Poland

²Institute for Computational Cosmology, Durham University, South Road, Durham, DH1 3LE, UK

³Carnegie Observatories, 813 Santa Barbara Street, Pasadena, CA 91101, U.S.A

Accepted XXX. Received YYY; in original form ZZZ

ABSTRACT

Low-mass galaxies provide a powerful tool with which to investigate departures from the standard cosmological paradigm in models that suppress the abundance of small dark matter structures. One of the simplest metrics that can be used to compare different models is the abundance of satellite galaxies in the Milky Way. Viable dark matter models must produce enough substructure to host the observed number of Galactic satellites. Here, we scrutinize the predictions of the neutrino Minimal Standard Model (ν MSM), a well-motivated extension of the Standard Model of particle physics in which the production of sterile neutrino dark matter is resonantly enhanced by a lepton asymmetry in the primordial plasma. This process enables the model to evade current constraints associated with non-resonantly produced dark matter. Independently of assumptions about galaxy formation physics we rule out, with at least 95 per cent confidence, all parameterizations of the ν MSM with sterile neutrino rest mass, $M_s \leq 1.4$ keV. Incorporating physically motivated prescriptions of baryonic processes and modelling the effects of reionization strengthen our constraints, and we exclude all ν MSM parameterizations with $M_s \leq 4$ keV. Unlike other literature, our fiducial constraints do not rule out the putative 3.55 keV X-ray line, if it is indeed produced by the decay of a sterile neutrino; however, some of the most favoured parameter space is excluded. If the Milky Way satellite count is higher than we assume, or if the Milky Way halo is less massive than $M_{200}^{\text{MW}} = 8 \times 10^{11} M_\odot$, we rule out the ν MSM as the origin of the 3.55 keV excess. In contrast with other work, we find that the constraints from satellite counts are substantially weaker than those reported from X-ray non-detections.

Key words: dark matter – elementary particles – Galaxy: halo – galaxies: dwarf – galaxies:formation

1 INTRODUCTION

Understanding the nature of dark matter is one of the greatest outstanding challenges in contemporary physics. In the prevailing cosmological framework known as Λ +cold dark matter (Λ CDM) most of the dark matter is typically composed of weakly interacting, massive fundamental particles (WIMPs) exhibiting negligible thermal velocities at early times (Peebles 1982; Davis et al. 1985; Bardeen et al. 1986). Although Λ CDM successfully predicts and replicates various observable features of the Universe, terrestrial direct detection (e.g. SuperCDMS Collaboration et al. 2015; CRESST Collaboration et al. 2019; DEAP Collaboration et al. 2019; PICO Collaboration et al. 2019; PandaX-4T Collaboration et al. 2021; Aalbers et al. 2023; Abe et al. 2023; Agnes et al. 2023; Aprile et al. 2023), indirect detection (Albert et al. 2017; H.E.S.S. Collaboration et al. 2018; Di Mauro et al. 2019; The Super-Kamiokande Collaboration et al. 2020; Regis et al. 2021; IceCube Collaboration et al. 2022; Di Mauro et al. 2023; McDaniel et al. 2024; Yin et al. 2024, also see Murgia 2020 for a comprehensive review of *Fermi* Large Area Telescope (*Fermi*–LAT) searches for a γ -ray excess), and particle collider searches (ATLAS Collaboration et al. 2021b,a; CMS Collaboration et al. 2021; Tumasyan et al. 2022b,a; Aad et al. 2023; Tumasyan et al. 2023) have

yet to establish that weakly interacting massive dark matter particles exist. This has encouraged closer examination of alternative dark matter models that are well motivated in the particle physics context and which may be compatible with the successes achieved on astrophysical scales by Λ CDM.

Astrophysical observations serve as critical benchmarks against which to evaluate various aspects of these alternative models. In particular, low-mass galaxies provide valuable insights into the physics governing the onset of structure formation and its subsequent evolution. It is within this regime that departures from the prevailing paradigm are likely to manifest. Models in which the dark matter is relativistic in the early Universe and undergoes free-streaming on scales that suppress the formation of low-mass haloes may struggle to account for the observed abundance of Milky Way satellite galaxies. This has proven to be an effective means of imposing stringent constraints on several ‘warm’ dark matter models (WDM, e.g. Kennedy et al. 2014; Lovell et al. 2016; Enzi et al. 2021; Nadler et al. 2021; Newton et al. 2021; Dekker et al. 2022). In this study we adopt this approach, described in detail in Newton et al. (2021), to impose constraints on the parameter space of one well-motivated model: the neutrino Minimal Standard Model (ν MSM).

The ν MSM, a minimal extension of the Standard Model of particle physics, introduces three ‘sterile’ neutrinos alongside the family of three standard model ‘active’ neutrinos (Shi & Fuller 1999; Asaka &

* E-mail: onewton@cft.edu.pl

Shaposhnikov 2005; Laine & Shaposhnikov 2008). The sterile neutrinos are produced by the oscillation of the left-chiral active neutrinos into right-chiral states, characterized by the mixing angle, θ . The mixing of the active and sterile neutrino states produces two distinct sets of mass eigenstates wherein the masses in one set increase as the neutrinos in the other set become less massive (Minkowski 1977; Gell-Mann et al. 1979; Barbieri et al. 1980; Mohapatra & Senjanović 1980; Yanagida 1980). This elegant mechanism offers a plausible explanation for the extremely small masses of the active neutrinos of the Standard Model. The high mass eigenstates are ascribed to the sterile neutrinos: one with a mass $\mathcal{O}(\text{keV})$ that is long-lived and exhibits relativistic behaviour up to nine years after the Big Bang (Lovell 2023), and two others with masses in the GeV scale that are unstable and extremely short-lived (Adhikari et al. 2017; for a detailed review see Abazajian et al. 2012). Their decay into anti-leptons introduces an asymmetry in the lepton abundance (Fukugita & Yanagida 1986) that is partially reprocessed into a baryon asymmetry during baryogenesis. This provides a natural explanation for the observed asymmetry of matter to anti-matter in the Universe (Shaposhnikov 2008; Canetti et al. 2012, 2013). A recent comprehensive description of the production mechanisms underpinning the νMSM in an astrophysical context is available in Lovell (2023).

As active neutrinos propagate through a medium their oscillation parameters may diverge from those *in vacuo* because of interactions with electrons in the medium. This phenomenon is known as the Mikheyev–Smirnov–Wolfenstein (MSW) effect (Wolfenstein 1978; Mikheyev & Smirnov 1985). An analogous mechanism within the primordial plasma affects the mixing of the active and sterile neutrino states in the νMSM . This is controlled by the size of the lepton asymmetries in different particle species, which can resonantly enhance the production of sterile neutrinos by increasing the effective mixing angle, θ_e (Laine & Shaposhnikov 2008). Through this process, the νMSM may generate sufficient numbers of long-lived keV scale sterile neutrinos to be consistent with the measured abundance of dark matter. Since the sterile neutrinos decouple from the primordial plasma before the onset of Big Bang nucleosynthesis they do not affect the primordial abundance of chemical elements. Consequently, astrophysical measurements of the elemental abundances, which have been used to constrain the properties of thermally produced WDM candidates, cannot be applied to constrain the νMSM parameter space (Sabti et al. 2020; An et al. 2022).

Efforts to ascertain the nature of the dark matter intensified in response to astrophysical spectroscopic observations revealing a possible spectral line at 3.55 keV in systems containing a significant dark matter component (Bulbul et al. 2014; Boyarsky et al. 2014; Cappelluti et al. 2018; Hofmann & Wegg 2019). This has elicited considerable interest, given the absence of a known astrophysical origin for a spectral line at this energy. While charge exchange between sulphur ions and a neutral medium could provide a plausible baryonic explanation (Gu et al. 2015; Shah et al. 2016), it cannot be confirmed with the resolution available in current instruments.¹ Moreover, it may be unable to account for all of the observed flux in any case (Cappelluti et al. 2018). The analysis of the excess is complicated further by the choice of assumptions embedded in the modelling of

the astrophysical background (Dessert et al. 2024b, also see Boyarsky et al. 2019 for a recent review).

A non-baryonic explanation for the excess could be provided by the dark sector. Interpreting the line as the decay product of a dark matter particle would place the rest mass of the parent particle within the range expected of a sterile neutrino candidate responsible for the entire dark matter component of the cosmic matter density. Follow-up observations of the spectral feature in the Galactic centre (Boyarsky et al. 2015; Perez et al. 2017; Hofmann & Wegg 2019), the Perseus cluster (Urban et al. 2015; Franse et al. 2016), and in other galaxy clusters (Bulbul et al. 2016, but see also Hofmann et al. 2016) have been carried out in attempts to improve the significance of the detection and elucidate the origin of the excess, with limited success. These plausible detections are challenging to reconcile with the non-detections reported by other observational studies of stacked galaxy spectra (Anderson et al. 2015), the Galactic centre (Riemer-Sørensen 2016), the Draco dwarf galaxy (Ruchayskiy et al. 2016; Sonbas et al. 2016), the X-ray background (Sekiya et al. 2016), and Perseus (Aharonian et al. 2017; Tamura et al. 2019). The origin of the 3.55 keV excess thus remains unclear, and this emphasizes the need for higher resolution measurements of the soft X-ray spectrum in dark matter-dominated systems. This will be achievable with the JAXA *XRISM* mission that launched in 2023 September that is now in the final stages of commissioning (Tashiro et al. 2018; Lovell et al. 2019a,b; Terada et al. 2021; Dessert et al. 2024a).

In this work, we impose constraints on the parameter space of resonantly produced νMSM models by comparing the predicted abundance of low-mass galaxies in Milky Way mass dark matter haloes with the inferred total population of Milky Way satellite galaxies. In Section 2, we summarize the method as applied to the νMSM and calibrate it using dark matter-only N -body simulations of νMSM models. We present our constraints on the νMSM parameter space in Section 3 and compare them with related studies. We discuss our results in Section 4 and present concluding remarks in Section 5.

2 METHODS

Newton et al. (2021) described an approach to constrain the parameter space of thermal relic WDM models by comparing predictions of the abundance of substructure in Milky Way mass dark matter haloes with the total number of satellite galaxies estimated from observations of the Milky Way halo. Here, we apply the same technique to constrain the viable combinations of the sterile neutrino rest mass, M_s , and the resonantly enhanced effective mixing angle, θ_e , in the νMSM . We make predictions of the abundance of substructure in different parameterizations of the νMSM using the Extended Press–Schechter formalism, first computing the νMSM momentum distributions and matter power spectra in Section 2.1, then using Extended Press–Schechter theory to predict the subhalo counts; we describe and calibrate the Extended Press–Schechter formalism using gravity only cosmological simulations of Milky Way mass haloes in Section 2.2. In Section 2.3, we summarize the approach we take to evaluate the viability of each parameterization of the model.

2.1 Computing the νMSM sterile neutrino power spectra

The primary goal of this study is to predict the abundance of satellites of galaxies like the Milky Way as a function of the dark matter model parameters. The first step is to compute the momentum distribution of the dark matter at an energy of 1 MeV, or approximately one second after the Big Bang, which is then input to a Boltzmann solver code

¹ The instruments onboard *Hitomi* filled this gap in capability prior to its rapid unscheduled disassembly. Unfortunately, the data collected were insufficient to draw definitive conclusions regarding charge exchange as the origin of the X-ray excess. The shortfall in spectral resolution will be rectified when the newly launched *XRISM* satellite starts taking performance verification data.

that calculates the linear matter power spectrum, $P(k)$. We compute momentum distributions for an array of 36 values of M_s and 31 values of the lepton asymmetry parameter, L_6 , using the code of [Laine & Shaposhnikov \(2008\)](#). The $P(k)$ are then calculated with a modified version of the CAMB Boltzmann solver ([Lewis et al. 2000](#)).

One of the key uncertainties in our results will be the accuracy of the momentum distribution calculation. The [Laine & Shaposhnikov \(2008\)](#) algorithm has been superseded by that of [Ghiglieri & Laine \(2015\)](#), with minor modifications to the free-streaming length. A further study by [Venumadhav et al. \(2016\)](#) produced results that differ significantly from those of [Ghiglieri & Laine \(2015\)](#): the former predicts a cut-off scale some three times larger than the latter at fixed sterile neutrino mass and effective mixing angle ([Lovell 2023](#)). We will discuss this discrepancy further in Section 3.3.

2.2 Calibrating the Extended Press–Schechter formalism with numerical simulations

In the Extended Press–Schechter formalism the primordial matter density field is filtered using a window function to identify regions that are dense enough to collapse into virialized haloes by the present day ([Press & Schechter 1974](#); [Bond et al. 1991](#); [Bower 1991](#); [Lacey & Cole 1993](#); [Parkinson et al. 2008](#)). The abundance of structure at different mass scales can be calculated from this using the conditional halo mass function, $dN_{\text{cond}}/d\ln M$. This describes the fraction of the mass in some halo at time, t_1 , that was in collapsed progenitors of a given mass, M , at some earlier time, t_2 . The conditional halo mass function depends on the primordial linear matter power spectrum, and its functional form and the details of its derivation are provided in [Schneider \(2015\)](#).

The subhalo mass function is computed by integrating the conditional halo mass function over the redshift-dependent overdensity collapse threshold of a given progenitor, $\delta_c(z)$. It is given by

$$\frac{dN_{\text{sub}}}{d\ln M} = \frac{1}{N_{\text{norm}}} \int_{\delta_c(0)}^{\infty} \frac{dN_{\text{cond}}}{d\ln M} d\delta_c, \quad (1)$$

where N_{sub} is the number of subhaloes within a given halo and N_{norm} is a normalization constant. The latter term, which is a free parameter that must be calibrated using simulations, corrects the total number count for progenitor subhaloes that exist at multiple redshifts. These structures are counted more than once in this approach ([Schneider 2015](#)). We calibrate N_{norm} at scales above the power spectrum cut-off to minimise any dependence on the shape of the power spectrum.

The form of the window function can affect the predictions of the mean number of subhaloes in a halo of a given mass. Customarily, using a spherical top-hat function in real space has been favoured because there is a simple relation between the filter volume, the filter scale radius, and the mass enclosed by the virialised object. Somewhat more importantly, this approach has also been shown to produce results that are in good agreement with those of numerical simulations of cold dark matter ([Jenkins et al. 2001](#)). However, for models of dark matter with power spectra that are damped at small scales, such as the ν MSM, this approach predicts an excess of low-mass haloes compared to numerical simulations ([Benson et al. 2013](#); [Schneider 2015](#)). This happens because the steep cut-off in the matter power spectrum permits only negligible contributions at high wavenumbers when calculating the variance of the matter density field in the limit of small radii. Meanwhile, in the same regime, the halo mass function is dominated by the derivative of the variance, which depends strongly on the form of the filter function that is used. Consequently, in dark matter models with damped power spectra, the halo mass function calculated when adopting a real space top-hat filter function

becomes independent of the power spectrum, and tends towards a constant value at small radii rather than becoming negligible. Instead adopting a smooth filter in k -space of the form,

$$\tilde{W}(k|R) = \left[1 + (kR)^{\hat{\beta}} \right]^{-1}, \quad (2)$$

where k is the wavenumber, R is the filter scale radius, and $\hat{\beta} > 0$ is a free parameter, results in better agreement with simulations ([Leo et al. 2018](#)). To achieve this good agreement, the smooth k -space filter introduces a second free parameter, \hat{c} , that connects the filter mass, M , to R through the mean density, $\bar{\rho}$, as $M(R) = 4\pi\bar{\rho}(\hat{c}R)^3/3$. Both $\hat{\beta}$ and \hat{c} , and the normalization constant that we discussed earlier, N_{norm} , must be calibrated with simulations. We showed in [Newton et al. \(2021\)](#) that using the Extended Press–Schechter formalism with a smooth k -space filter calibrated using a subset of haloes from the COCO suite ([Bose et al. 2016](#); [Hellwing et al. 2016](#)) produces results in good agreement with the simulations.

In this work we calibrate the Extended Press–Schechter and filter function parameters using gravity only counterparts of the ‘V2’ and ‘V5’ sets of Local Group-analogue simulations introduced by [Lovell et al. \(2017\)](#). Each set comprises a cold dark matter volume and two $M_s = 7$ keV ν MSM volumes with $\sin^2(2\theta_e) \simeq 10^{-11}$. They were simulated using initial conditions that are identical to the first six simulation volumes of the APOSTLE project ([Fattahi et al. 2016](#); [Sawala et al. 2016](#)), except for the differences introduced by changing the properties of the dark matter. All simulations adopt cosmological parameters from the WMAP seventh-year data release ([Komatsu et al. 2011](#)): $H_0 = 70.4$ km s $^{-1}$ Mpc $^{-1}$, $\Omega_M = 0.272$, $\Omega_\Lambda = 0.728$, $n_s = 0.967$, $\sigma_8 = 0.81$.

Simulations of dark matter models that impose a cut-off in the primordial power spectrum are susceptible to the formation of ‘spurious’ haloes. These structures are produced by the artificial fragmentation of filaments caused by resolution-dependent gravitational instabilities that are generated by the discreteness of the simulation particles ([Wang & White 2007](#); [Angulo et al. 2013](#); [Lovell et al. 2014](#)). We identify and prune spurious haloes from the merger trees by adopting the procedure introduced by [Lovell et al. \(2014\)](#), which we summarize here. Numerical gravitational instabilities emerge when the gravitational potential is sampled poorly by simulation particles. The onset of these instabilities is associated with a resolution-dependent mass threshold, and haloes that do not surpass this during their evolution are likely to be spurious. In addition, spurious haloes typically form from highly aspherical Lagrangian regions in the initial conditions. These regions are characterized using the particles that compose the halo when it accumulates half of its maximum mass. The shapes of the Lagrangian regions are parameterized by $s_{\text{half-max}} = c/a$, where c and a are, respectively, the minor and major axes of the diagonalized moment of inertia tensor of the dark matter particles in Lagrangian coordinates. The threshold mass and $s_{\text{half-max}}$ values for the ν MSM APOSTLE are calculated in the appendix of [Lovell et al. \(2017\)](#), who found that almost all spurious haloes can be removed by requiring $M_{\text{max}} > 5.35 \times 10^7 h^{-1} M_\odot$ and $s_{\text{half-max}} > 0.165$. We adopt these thresholds to prune the ν MSM APOSTLE simulations we consider in Fig. 1.

We also correct for other resolution-dependent effects. It has been shown that configuration-space structure finders fail to identify some small haloes that clearly survive to the present day. Subhaloes that are close to the centre of the host halo are particularly likely to be overlooked. Additionally, some small haloes are artificially disrupted by tidal forces due to numerical effects such as small particle number. We recover all prematurely destroyed subhaloes by tracking their most-bound particles through the simulations and determining

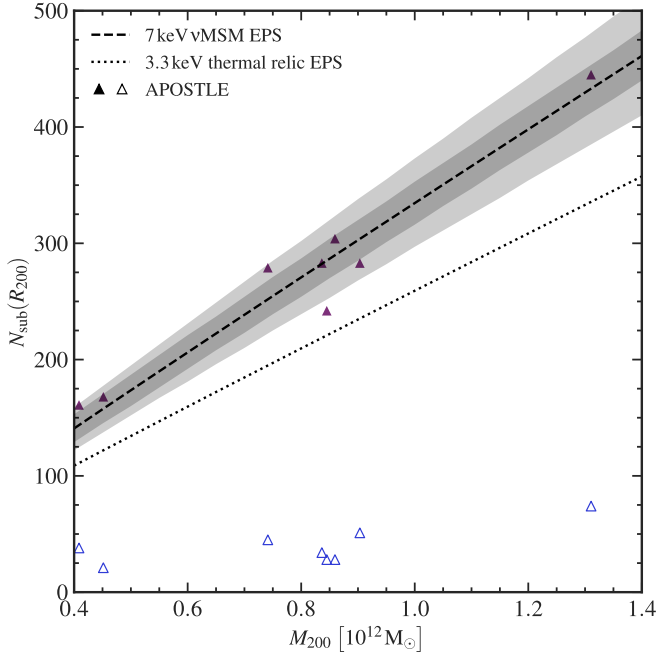


Figure 1. The total number of dark matter subhaloes within R_{200} as a function of dark matter halo mass, M_{200} . Need to state which nuMSM model parameters these are. The dashed line shows the mean number of subhaloes predicted by the Extended Press–Schechter formalism when adopting the ν MSM parameters $M_s = 7.1$ and $\sin^2(2\theta_e) \approx 10^{-11}$. The dark shaded region indicates the associated 68 per cent Poisson scatter, and the light shaded region gives the 68 per cent scatter modelled using a negative binomial distribution (see equation 3). The symbols represent haloes from the 7 keV ν MSM APOSTLE simulations for $\sin^2(2\theta_e) \approx 10^{-11}$. Unfilled symbols are from subhalo catalogues where the prematurely destroyed subhaloes have not been recovered, and filled symbols show the same haloes after the prematurely destroyed subhaloes have been restored by following the procedure described in Section 2.2. For comparison, we plot as a dotted line the number of subhaloes predicted by the Extended Press–Schechter formalism applied to the 3.3 keV thermal relic WDM model from Newton et al. (2021).

whether they survive to the present day. To do this we use the Simha & Cole (2017) merging scheme implemented in the galaxy formation model GALFORM (Cole et al. 2000) that recovers the entire population of destroyed substructures, including objects that were disrupted by physical processes. We identify and remove the latter from the recovered population if they satisfy one of the following criteria:

- The dynamical friction timescale, i.e. the time required for a subhalo to sink to the centre of the host halo, is less than or equal to the time elapsed since the subhalo fell below the resolution limit.
- The subhalo passes within the halo tidal disruption radius.

In both cases, the effects of tidal stripping and of interactions between other subhaloes are ignored. This procedure is discussed in more detail in Newton et al. (2021), appendix A.

After pruning spurious haloes from the merger trees and recovering the prematurely destroyed subhaloes, we obtain excellent agreement between the Extended Press–Schechter predictions and the ν MSM APOSTLE N -body results using $N_{\text{norm}} = 1.4$, $\hat{\beta} = 4.2$, and $\hat{c} = 3.9$. These values are very similar to the values we found in Newton et al. (2021) when calibrating the Extended Press–Schechter formalism for thermal relic WDM. In Fig. 1 the dashed line shows the mean number of subhaloes predicted by the Extended Press–Schechter formalism within R_{200} of the centre of Milky Way mass dark matter haloes

in the $M_s = 7.1$ keV, $\sin^2(2\theta_e) \approx 10^{-11}$ parameterizations of the ν MSM. Here and throughout the rest of this paper, M_{200} denotes the mass enclosed within R_{200} , the radius within which the mean density equals 200 times the critical density. The shaded regions represent the 68 per cent scatter in N_{sub} at fixed halo mass modelled using a negative binomial distribution, which encapsulates the scatter seen in numerical simulations (Boylan-Kolchin et al. 2010). This is given by

$$P(N|r, p) = \frac{\Gamma(N+r)}{\Gamma(r)\Gamma(N+1)} p^r (1-p)^N, \quad (3)$$

where $\Gamma(x) = (x-1)!$ and N is the number of subhaloes. The parameter, $p = \langle N \rangle / \sigma^2$, where $\langle N \rangle$ and $\sigma^2 = \sigma_{\text{Poisson}}^2 + \sigma_I^2$ are, respectively, the mean and the dispersion of the distribution. The parameter, $r = \sigma_{\text{Poisson}}^2 / \sigma_I^2$, describes the relative contribution of Poisson fluctuations compared to a second distribution that describes the intrinsic variability of the subhalo count within haloes of fixed mass. We model the scatter in the subhalo count by adopting $\sigma_I = 0.12\langle N \rangle$, which is in good agreement with that found in N -body simulations such as COCO (Newton et al. 2021). In Fig. 1, we also overlay the subhalo counts of Milky Way mass haloes in the APOSTLE $M_s = 7$ keV, $\sin^2(2\theta_e) \approx 10^{-11}$ simulations, both before and after restoring the population of prematurely destroyed subhaloes to the catalogues. The Extended Press–Schechter predictions and model of the scatter in the subhalo counts are in excellent agreement with the latter.

At fixed mass, the Milky Way mass haloes that form in the parameterization of the ν MSM shown in Fig. 1 (dashed line) are predicted to host more dark matter subhaloes than they would in the 3.3 keV thermal relic WDM model (dotted line). Consequently, larger fractions of the ν MSM systems host at least as many subhaloes as the inferred total Milky Way satellite galaxy population. As Newton et al. (2021) were unable to place constraints on the 3.3 keV thermal relic model using this approach, we will be similarly unable to constrain the $\sin^2(2\theta_e) \approx 10^{-11}$ parameterizations of the $M_s = 7.1$ keV ν MSM model. We will discuss our full results in Section 3.1.

2.3 Calculating model acceptance probability

We obtain our constraints on the ν MSM parameter space by following the approach described in Newton et al. (2021), which we summarize briefly here. First, we calculate the fraction, f_v , of Milky Way mass systems that have at least as many satellites $N_{\text{sat}}^{\nu\text{MSM}}$, as the total number of Milky Way satellite galaxies, $N_{\text{sat}}^{\text{MW}}$, for a given set of ν MSM parameters. This is given by

$$f_v = \int_0^\infty dN_{\text{sat}}^{\text{MW}} p^{\text{MW}}(N_{\text{sat}}^{\text{MW}}) \times \int_{N_{\text{sat}}^{\text{MW}}}^\infty dN_{\text{sat}}^{\nu\text{MSM}} p^{\nu\text{MSM}}(N_{\text{sat}}^{\nu\text{MSM}}), \quad (4)$$

where p^{MW} and $p^{\nu\text{MSM}}$ are, respectively, the probability distributions of the Milky Way satellite count, and of the number of satellites predicted to be hosted by Milky Way mass haloes at $z = 0$ in a given parameterization of the ν MSM model. Then, we obtain constraints by computing the intersection of the cumulative distribution of f_v as a function of Milky Way halo mass at fixed M_s and θ_e with a five per cent rejection threshold. Parameterizations of the ν MSM at and below this threshold are ruled out.

Our calculation of f_v in equation (4) accounts for the scatter in the number of dark matter subhaloes at fixed host halo mass and the uncertainty in the size of the total Milky Way satellite galaxy

population. As both of these quantities depend on the assumed mass of the Galactic halo, the viable fraction is also highly sensitive to it. Estimates of the mass of the Galactic halo are still quite uncertain; indeed, it has been revised downwards in recent years (see e.g. Bird et al. 2022). To account for this uncertainty we calculate f_ν for several Milky Way halo masses spanning the most likely range determined from kinematic analyses of the Galactic potential. Unless stated otherwise the constraints we present in Section 3 are marginalized over the distribution of Milky Way halo masses from Callingham et al. (2019).

3 CONSTRAINTS ON THE PROPERTIES OF STERILE NEUTRINOS IN THE ν MSM

The constraints on the parameter space of the ν MSM depend on the assumed mass of the Milky Way halo, the rest mass of the sterile neutrino dark matter candidate, M_s , and the resonantly enhanced effective mixing angle of the sterile neutrino, θ_e . We consider Milky Way halo masses in the likely range $M_{200}^{\text{MW}} = (0.5\text{--}2.0) \times 10^{12} M_\odot$ (Callingham et al. 2019; Cautun et al. 2020), and values of $\sin^2(2\theta_e)$ between the dark matter under- and over-production bounds if the sterile neutrino comprises all of the dark matter. In this and subsequent sections we assume the Planck Collaboration et al. (2020) cosmology: $H_0 = 67.4 \pm 0.5 \text{ km s}^{-1} \text{ Mpc}^{-1}$, $\Omega_M = 0.315 \pm 0.007$, $\Omega_\Lambda = 0.685 \pm 0.007$, $n_s = 0.965 \pm 0.004$, $\sigma_8 = 0.811 \pm 0.006$. For each combination of parameters, we compute the fraction of ν MSM systems that produce at least as many galaxies as the number of Milky Way satellite galaxies inferred from observations using the methodology presented in Newton et al. (2018), as implemented in Newton & Cautun (2018).

We obtain our most robust result, presented in Section 3.1, under the premise that all dark matter subhaloes host a visible galaxy; therefore, we make no assumptions at all about galaxy formation processes. This maximises f_ν and produces extremely robust lower limits on the viable ν MSM parameter space. In Section 3.2, we use the GALFORM semi-analytic model of galaxy formation to estimate the number of satellite galaxies in each parameterization of the ν MSM. This allows us to account for astrophysically relevant processes, such as reionization, that can affect the properties of the low-mass galaxy population. In Section 3.3, we consider how our results are affected when we use different estimates of $N_{\text{sat}}^{\text{MW}}$ from that reported by Newton et al. (2018) and compare these results with others in recent literature.

3.1 Constraints from structure formation considerations

In Fig. 2, we present constraints on the parameter space of ν MSM models obtained by comparing the abundance of dark matter substructure predicted using the Extended Press–Schechter formalism with the Newton et al. (2018) number count of Milky Way satellite galaxies. Parameter combinations of M_s and θ_e within the shaded regions are ruled out with at least 95 per cent confidence when marginalizing over the uncertainties in the Milky Way halo mass from Callingham et al. (2019). We show recent astrophysical limits from X-ray modelling of M31 (Horiuchi et al. 2014), Galactic bulge non-detections (Roach et al. 2020), and blank sky non-detections (Dessert et al. 2020b; Foster et al. 2021; Roach et al. 2023) using a dark grey curve and shaded region. The viable parameter space decreases significantly at and below $M_s = 7 \text{ keV}$, and we rule out all parameterizations of the ν MSM with $M_s \leq 1.2 \text{ keV}$. This result is

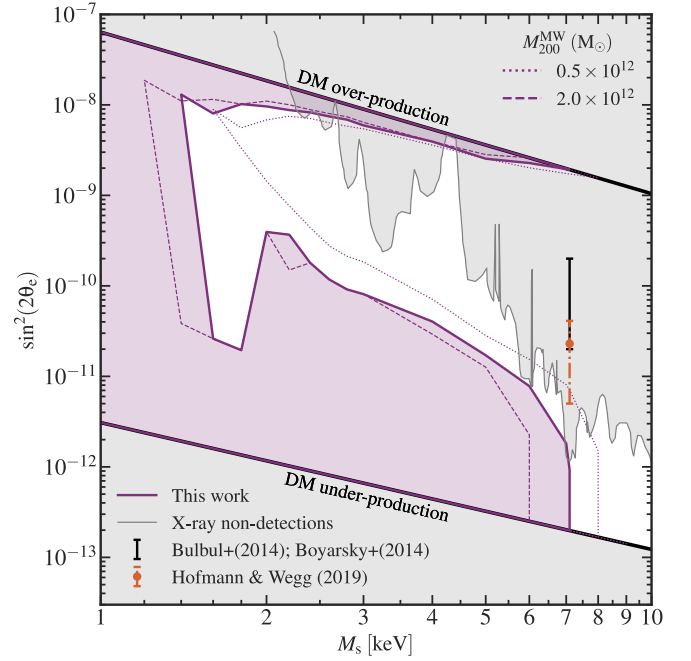


Figure 2. Constraints on the ν MSM parameter space obtained assuming all subhaloes host a galaxy. Our fiducial structure count result (thick solid curve) is marginalized over the uncertainties in the Callingham et al. (2019) estimate of the Milky Way halo mass. Parameter combinations in the shaded region to the left of this envelope are ruled out with at least 95 per cent confidence. We also show the constraint envelopes we obtain assuming Milky Way halo masses of $M_{200}^{\text{MW}} = 0.5 \times 10^{12} M_\odot$ (dotted curve) and $M_{200}^{\text{MW}} = 2.0 \times 10^{12} M_\odot$ (dashed curve). The shaded regions in the upper and lower portions of the parameter space delimit parameter combinations for which the dark matter is over- or under-produced compared with current observational estimates of the composition of the Universe if resonantly produced sterile neutrinos compose all of the dark matter (Asaka et al. 2005; Schneider 2016). The lower limits on the effective mixing angle obtained from X-ray non-detections are shown using the thin solid curve and shading (Neronov et al. 2016; Ng et al. 2019; Roach et al. 2020, 2023). The solid error bar indicates the parameter range favoured by X-ray flux measurements if the dark matter consists of $M_s = 7.1 \text{ keV}$ decaying sterile neutrinos (Boyersky et al. 2014; Bulbul et al. 2014). The dash-dot error bar shows the preferred range determined from X-ray line detections in the Galactic bulge (Hofmann & Wegg 2019).

valid for all Milky Way halo masses we consider up to and including the largest mass of $M_{200}^{\text{MW}} = 2 \times 10^{12} M_\odot$ (dashed curve), which produces the least constraining results. When marginalizing over the uncertainty in the Callingham et al. (2019) estimate of the Milky Way halo mass, we rule out all parameterizations of the ν MSM with $M_s \leq 1.4 \text{ keV}$. These results are consistent with constraints obtained by theoretical and observational analyses of the phase space density of dark matter within Milky Way dwarf satellite galaxies (Boyersky et al. 2009).

As we discussed in Section 1, the 3.55 keV excess observed emanating from several dark matter-rich astrophysical systems could potentially be evidence of decaying ν MSM sterile neutrinos with rest masses, $M_s = 7.1 \text{ keV}$. If all of the dark matter in the Universe is composed of these ν MSM neutrinos, X-ray flux observations favour a narrow window of viable parameter space (Boyersky et al. 2014, 2015; Bulbul et al. 2014; Iakubovskiy et al. 2015; Ruchayskiy et al. 2016). We indicate this in Fig. 2 using a solid error bar. We also show the preferred region of parameter space determined from X-ray line detections in the Galactic bulge (Hofmann & Wegg 2019)

using a dash-dot error bar. Our fiducial results, which we emphasize make no assumptions about galaxy formation physics, constrain the $M_s = 7.1$ keV ν MSM parameter space only at small values of θ_e because the amount of substructure produced by other parameterizations is too great. If the mass of the Milky Way is at the lower end of estimates (dotted curve), as suggested by recent studies (e.g. Bird et al. 2022; Necib & Lin 2022; Zhou et al. 2023; Roche et al. 2024), more of the parameter space is excluded, including some parameterizations favoured by Hofmann & Wegg (2019). The limits from X-ray non-detections already exclude the ν MSM as a viable explanation for the origin of the 3.55 keV excess, although they are subject to modelling uncertainty (Dessert et al. 2020b, though see Abazajian 2020; Boyarsky et al. 2020, and Dessert et al. 2020a). Combining this exclusion region with our fiducial satellite count constraints, all parameterizations of the ν MSM with $M_s = 7.1$ keV are excluded. This conservative and highly robust result can be extended to more of the parameter space by adopting a physically motivated prescription to populate some of the subhaloes with galaxies. This reduces the subhalo occupation fraction and, consequently, strengthens the constraints on the viable parameter space of favoured models. We explore this in Section 3.2.

Our analysis depends on the total number of Milky Way satellite galaxies, which is uncertain. In Appendix A, we present the structure count constraints we obtain when assuming different values of the size of the total Milky Way satellite galaxy population that have been proposed in recent years. We will discuss this within the context of applying a galaxy formation model in Section 3.3.

3.2 Modelling galaxy formation processes

The satellite count constraints presented in Section 3.1 are highly robust and conservative lower limits on the ν MSM parameter space. However, they ignore the effects of baryon physics on the formation and evolution of the stellar component in low-mass haloes. Although the details of these processes are not fully understood they are expected to have a significant effect on the properties of the satellite galaxy population of the Milky Way. To understand how baryonic physics affects the constraints we explore the parameter space of these processes using the GALFORM semi-analytic model of galaxy formation (Cole et al. 1994, 2000; Lacey et al. 2016). The parameters of this state-of-the-art model are calibrated to reproduce a variety of observational results, including the $z = 0$ luminosity functions of galaxies in the local Universe, the HI mass function, the distributions of galaxy morphologies and sizes, the $z = 0$ Tully–Fisher relation, and the number counts of sub-millimeter galaxies. The complete set of observations used to calibrate the GALFORM model parameters is described in Lacey et al. (2016, section 4.2). Although GALFORM has been calibrated assuming the Λ CDM model, it is not necessary to recalibrate it for each parameterization of the ν MSM. This is because GALFORM is calibrated using massive galaxies far above the mass scales relevant here, and we do not expect that changes in the small-scale dark matter distribution will affect the outcome.

Among the various astrophysical processes that can be explored with GALFORM, the effect of the reionization of the Universe on low-mass galaxies is of particular interest for this study. During reionization the intergalactic medium is heated by the UV background radiation and is prevented from cooling into low-mass haloes. This inhibits the accretion of fresh supplies of cold gas that are necessary for star formation, thereby curtailing further growth of the stellar component. In GALFORM this is modelled by assuming that after reionization finishes at redshift, $z = z_{\text{reion}}$, gas cooling does not take place in haloes with circular velocities, $V_{\text{circ}} < V_{\text{cut}}$. In general, more

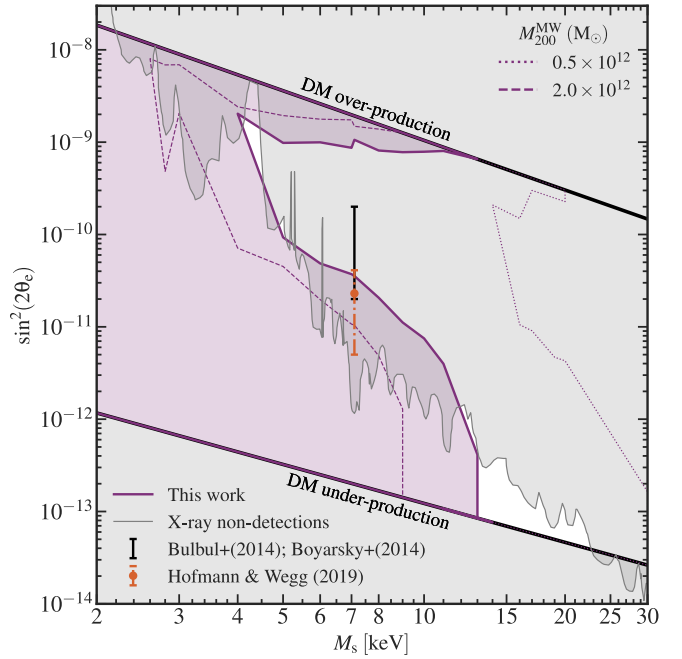


Figure 3. Constraints on the ν MSM parameter space obtained assuming our fiducial model of reionization ($z_{\text{reion}} = 7$ and $V_{\text{cut}} = 30 \text{ km s}^{-1}$) in the GALFORM galaxy formation model. Our main result marginalizes over the uncertainties in the Callingham et al. (2019) estimate of the Milky Way halo mass (thick solid curve). Parameter combinations in the shaded region to the left of this envelope are ruled out with at least 95 per cent confidence. We also show the constraint envelopes we obtain assuming Milky Way halo masses of $M_{200}^{\text{MW}} = 0.5 \times 10^{12} M_{\odot}$ (dotted curve) and $M_{200}^{\text{MW}} = 2.0 \times 10^{12} M_{\odot}$ (dashed curve). As in Fig. 2, the parameter space is delimited by upper and lower shaded regions in which the dark matter is over- or under-produced compared with current observational estimates of the composition of the Universe (Asaka et al. 2005; Schneider 2016). Lower limits on the effective mixing angle obtained from X-ray non-detections are shown using the thin solid curve and shading (Neronov et al. 2016; Ng et al. 2019; Roach et al. 2020, 2023). The solid and dot-dashed error bars indicate the parameter ranges favoured by X-ray flux measurements from different systems if all of the dark matter comprises $M_s = 7.1$ keV sterile neutrinos (Boyarsky et al. 2014; Bulbul et al. 2014; Hofmann & Wegg 2019).

low-luminosity galaxies are able to form if reionization finishes later, and lower values of the circular velocity cooling threshold, V_{cut} , permit those galaxies to become brighter because they are able to continue accreting gas for longer (e.g. Bose et al. 2018). Consequently, we expect to find the most stringent constraints on the ν MSM in the parameterizations of GALFORM where reionization finishes at higher redshifts and V_{cut} is large. Following the approach of Newton et al. (2021), we explore the parameter space of reionization spanning all combinations of $z_{\text{reion}} = [6, 7, 8]$ and $V_{\text{cut}} = [25, 30, 35] \text{ km s}^{-1}$.

To obtain constraints on the ν MSM, we generate predictions of the number of satellite galaxies brighter than $M_V = 0$ in Milky Way mass haloes and compare them with estimates of the total Milky Way satellite complement based on observations (Newton et al. 2018). We adopt the Lacey et al. (2016) version of the GALFORM model, which provides a reasonable description of a large variety of baryonic feedback and evolutionary processes, including those that are particularly relevant for low-mass galaxies such as star formation; gas heating and cooling; supernovae feedback; and the chemical enrichment of stars and gas; and vary the reionization parameters as described above. We generate Monte Carlo merger trees using an improved version of the Parkinson et al. (2008) algorithm, which we calibrate to match as

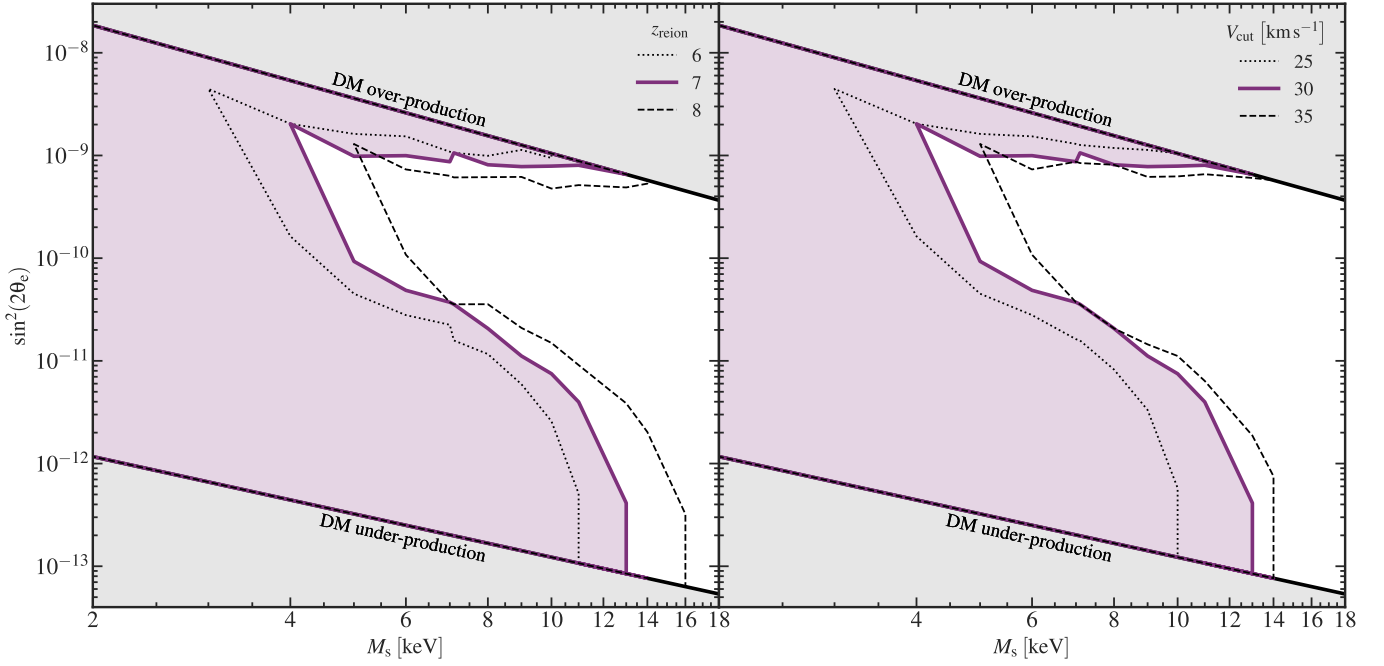


Figure 4. Constraints on the ν MSM parameter space obtained assuming different parameterizations of reionization in the GALFORM galaxy formation model when marginalizing over the uncertainties in estimates of the Milky Way halo mass from Callingham et al. (2019). Parameter combinations to the left of the envelopes are ruled out with at least 95 per cent confidence. In both panels our fiducial result is indicated by the thick solid curve and shaded region. *Left panel:* The circular velocity cooling threshold is fixed at $V_{\text{cut}} = 30 \text{ km s}^{-1}$ and we compute constraint envelopes assuming reionization finishes at $z_{\text{reion}} = 6$ (dotted curve), $z_{\text{reion}} = 7$ (solid curve), and $z_{\text{reion}} = 8$ (dashed curve). Parameterizations in which reionization finishes earlier produce more stringent constraints on the ν MSM parameter space. *Right panel:* The redshift at which reionization finishes is fixed at $z_{\text{reion}} = 7$ and we compute constraint envelopes assuming circular velocity cooling thresholds of $V_{\text{cut}} = 25 \text{ km s}^{-1}$ (dotted curve), 30 km s^{-1} (solid curve), and 35 km s^{-1} (dashed curve). Higher cooling thresholds produce more stringent constraints on the ν MSM parameter space.

closely as possible the merger trees obtained from recent cold dark matter N -body simulations (A. J. Benson et al., in preparation). In Newton et al. (2021) we noted that the match to the N -body results at the faint end is inexact because the algorithm lacks sufficient free parameters to model both the high- and low-mass ends of the mass function. Here, we try to address this by modifying the Parkinson et al. (2008) algorithm to include an explicit dependence on the linear growth-rate factor and the logarithmic slope of the $\sigma(M)$ relation, which describes the variance of the matter density field as a function of mass. This introduces three new free parameters that we calibrate using N -body simulations. We provide full details of our modifications to the merger tree algorithm in Appendix B. Our alterations significantly improve the agreement between the Monte Carlo satellite galaxy luminosity functions and the N -body results; however, they are still slightly discrepant. Therefore, we adopt the approach described in Newton et al. (2021) and introduce an empirical correction to remap the M_V values of the Monte Carlo satellite galaxies to new values so that the resulting luminosity functions are consistent with those from the N -body simulations. Although we cannot eliminate the need to apply an empirical correction, the modifications we make to the Parkinson et al. (2008) algorithm reduce the size of the correction we must introduce when compared with that required in Newton et al. (2021). These are typically 10 per cent.

To generate the constraints on the ν MSM we produce satellite galaxy luminosity functions for 500 realizations of each Milky Way halo mass that we consider and use them to calculate the model acceptance distributions in the manner we described in Section 2.3. Parameterizations of the model for which no more than 5 per cent of the realizations have at least as many satellite galaxies as the obser-

vations are ruled out. In Fig. 3, the shaded exclusion region shows the constraints we obtain on the ν MSM parameter space using our fiducial model of reionization with $z_{\text{reion}} = 7$ and $V_{\text{cut}} = 30 \text{ km s}^{-1}$ when marginalizing over the uncertainties in the Milky Way halo mass from Callingham et al. (2019). Parameter combinations in this region are ruled out with at least 95 per cent confidence. Once again, we show the constraint envelopes for our fiducial parameterization of reionization assuming Milky Way halo masses at the lower (dotted curve) and upper (dashed curve) ends of the likely range. Independently of Milky Way halo mass, all parameterizations of the ν MSM with $M_s \leq 2.6 \text{ keV}$ are excluded by the Milky Way satellite count constraints with at least 95 per cent confidence (dashed curve). When marginalizing over possible Milky Way halo masses, almost all of the $M_s = 7.1 \text{ keV}$ ν MSM parameter space favoured by Hofmann & Wegg (2019) as an explanation for the 3.55 keV line, and some of the parameter space favoured by Bulbul et al. (2014) and Boyarsky et al. (2014), is excluded. These constraints complement the reported X-ray non-detection lower limits in closing the $M_s = 7.1 \text{ keV}$ ν MSM parameter space. If the Milky Way mass is $M_{200}^{\text{MW}} = 0.5 \times 10^{12} M_\odot$, we rule out all parameterizations of the ν MSM with $M_s \leq 14 \text{ keV}$. All parameterizations of the ν MSM with $M_s = 7.1 \text{ keV}$ are ruled out when $M_{200}^{\text{MW}} \leq 8 \times 10^{11} M_\odot$ (not shown).

We explore how changing the parameterization of reionization affects the constraints in Fig. 4. The left panel shows the effect of varying the redshift at which reionization finishes while holding the circular velocity cooling threshold fixed at $V_{\text{cut}} = 30 \text{ km s}^{-1}$. A late-finishing epoch of reionization (dotted curve) enables more galaxies to form in low-mass dark matter haloes and weakens the constraints on the ν MSM parameter space. This is most pronounced

in parameterizations of the ν MSM with $M_s \geq 10$ keV, where the parameter space is almost completely unconstrained. In the scenario in which reionization finishes earlier (dashed curve) than our fiducial choice the viable parameter space closes slightly, and all parameterizations below $M_s = 5$ keV are excluded. The right panel shows the constraints for scenarios in which reionization finishes at $z_{\text{reion}} = 7$. Lowering the circular velocity cooling threshold permits a larger fraction of the low-mass galaxy population to accrete fresh supplies of cold gas after the end of reionization. This is then available to fuel further star formation that causes the faintest galaxies to become brighter than $M_V = 0$ by $z = 0$. The brightened galaxies populate the satellite galaxy luminosity function of the halo and weaken the constraints on the ν MSM parameter space (dotted curve). Raising V_{cut} has the opposite effect, and a larger fraction of the low-mass galaxies may only form stars from the reservoir of cold gas accreted prior to reionization. This limits how bright they become by $z = 0$, and fewer of them become brighter than $M_V = 0$ to populate the luminosity function. Consequently the constraints become stronger in this case (dashed curve). Similarly to the left panel, parameterizations of the ν MSM with sterile neutrino rest masses larger than $M_s = 10$ keV are particularly sensitive to changes to the circular velocity cooling threshold.

3.3 Dependence on the total number of Milky Way satellite galaxies

Recent improvements in the quantity and quality of observations of the Milky Way satellite system have motivated renewed efforts to estimate the size of the total population, $N_{\text{sat}}^{\text{MW}}$. This number remains highly uncertain because current observations are insufficiently deep to probe as far as the virial radius of the Milky Way halo, and they do not cover the entire sky. As analyses such as ours depend on $N_{\text{sat}}^{\text{MW}}$ it is important to understand how the results are affected when assuming different values. This is especially important when comparing our results with other studies that implement the same technique to impose constraints on the parameter space of the ν MSM (Nadler et al. 2021). In Fig. 5, we present the constraints derived from our fiducial GALFORM model ($z_{\text{reion}} = 7$ and $V_{\text{cut}} = 30 \text{ km s}^{-1}$) while adopting three different estimates of the size of the Milky Way satellite galaxy population from recent literature (Newton et al. 2018; Nadler et al. 2019, 2020). As in previous sections we have marginalized over the uncertainties in the Callingham et al. (2019) estimate of the Milky Way halo mass. Our constraints become more restrictive as the assumed value of $N_{\text{sat}}^{\text{MW}}$ increases because the ν MSM models must produce more substructure containing galaxies to remain viable. Adopting $N_{\text{sat}}^{\text{MW}} = 134$ (dashed curve) as suggested by Nadler et al. (2019), a value that is slightly larger than the Newton et al. (2018) estimate we used for our fiducial results in Sections 3.1 and 3.2, yields little change in the constraints for parameterizations of the ν MSM with $M_s = 7.1$ keV. If the total satellite population is closer to $N_{\text{sat}}^{\text{MW}} = 183$ (dotted curve), as suggested by Nadler et al. (2020), we find that the viable parameter space of the ν MSM decreases significantly, in agreement with Nadler et al. (2021). Moreover, the currently favoured parameter space of plausible ν MSM models corresponding to the putative 3.55 keV X-ray excess closes completely.

Alongside our constraints in Fig. 5, we plot the constraint envelopes reported by Nadler et al. (2021), who adopt the estimates of the size of the Milky Way satellite galaxy population mentioned above. At fixed $N_{\text{sat}}^{\text{MW}}$ their constraints are more stringent than ours. A comparison between our results is complicated by various factors. To begin with, Nadler et al. (2021) do not calculate constraints on the

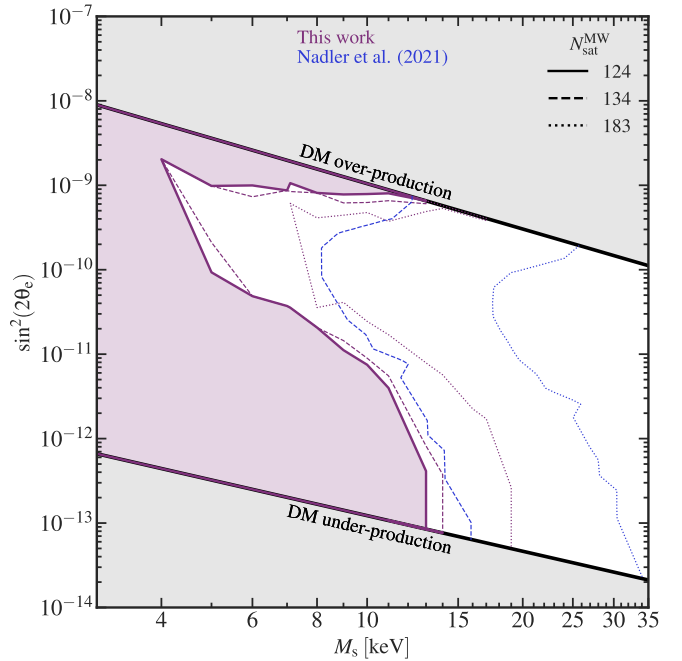


Figure 5. Constraints on the ν MSM parameter space from analyses of Milky Way satellite counts. The shaded regions in the upper and lower portions of the parameter space delimit parameter combinations for which the dark matter is over- or under-produced compared with current observational estimates of the composition of the Universe if resonantly produced sterile neutrinos compose all of the dark matter (Asaka et al. 2005; Schneider 2016). Our results adopt our fiducial model of reionization ($z_{\text{reion}} = 7$ and $V_{\text{cut}} = 30 \text{ km s}^{-1}$) in the GALFORM galaxy formation model marginalized over the uncertainties in estimates of the Milky Way halo mass from Callingham et al. (2019). We compute constraint envelopes assuming a total Milky Way satellite galaxy population with a mean value of $N_{\text{sat}}^{\text{MW}} = 124$ (thick solid curve), 134 (dashed curve), 183 (dotted curve), and 270 (dot-dashed curve). Parameter combinations within the envelopes are ruled out with at least 95 per cent confidence. For comparison we also show the constraint envelopes from Nadler et al. (2021).

ν MSM directly but rather infer them indirectly from constraints on the mass of a thermal relic neutrino.

There are several other differences between the two analyses. Nadler et al. (2021) adopt the Venumadhav et al. (2016) computation of the momentum distributions, which results in systematically larger cut-offs in the primordial power spectra at fixed sterile neutrino parameters than the Laine & Shaposhnikov (2008) algorithm that we use (Lovell 2023). Nadler et al. make use of subhalo abundance matching and several analytic prescriptions to populate a subset of subhaloes with galaxies in simulations of *thermal relic* neutrinos. They compare this with their estimate of $N_{\text{sat}}^{\text{MW}}$, which they determine using a forward modelling framework that accounts for the tidal influence of the LMC on the Milky Way halo, to obtain a constraint on the thermal relic WDM parameter space. They express this result in terms of the half-mode mass, M_{hm} , which is the mass corresponding to the half-mode scale, k_{hm} , at which the thermal relic power spectrum, P_{WDM} , is suppressed by a factor of four relative to the cold dark matter power spectrum, P_{CDM} (Viel et al. 2013; Bose et al. 2016), in other words, the scale at which

$$\sqrt{\frac{P_{\text{WDM}}(k_{\text{hm}})}{P_{\text{CDM}}(k_{\text{hm}})}} = 0.5. \quad (5)$$

Nadler et al. (2021) remap their thermal relic constraint to the ν MSM parameter space by comparing M_{hm} computed for each parameter-

ization of the ν MSM to that of the coldest permitted thermal relic power spectrum, and rule out those parameterizations where M_{hm} is greater than that of the thermal relic model.

The indirect approach followed by [Nadler et al. \(2021\)](#) is not directly comparable with our method. However, the stringency of their constraints suggests that their combination of subhalo abundance matching and analytic prescriptions suppresses the formation of low-mass galaxies more aggressively than the `GALFORM` prescription we adopt. As we discuss in detail in Section 4, this may be connected to the fixed mass threshold [Nadler et al.](#) employ to determine whether a galaxy is able to form in a given (sub)halo. Somewhat surprisingly, even when we adopt extremely high values of $N_{\text{sat}}^{\text{MW}}$ we are unable to replicate the stringency of their constraints obtained using smaller values. Some of this discrepancy could be explained by our choice to use the [Newton et al. \(2018\)](#) probability distribution to describe the uncertainty in $N_{\text{sat}}^{\text{MW}}$, which is broader than that of [Nadler et al. \(2020\)](#) on which the constraints reported in [Nadler et al. \(2021\)](#) are based. Broader uncertainties on $N_{\text{sat}}^{\text{MW}}$ can weaken the constraints by up to 15 per cent (see [Newton et al. 2021](#), section 2.4). However, the size of the discrepancy between the results of the two analyses suggests that this is a subdominant effect.

While a detailed investigation of the sources of disparity between the two studies is beyond the scope of this work, as we will see in Section 4, the methodological disparities in populating subhaloes with galaxies likely play a significant role alongside uncertainties in the particle physics calculation. The results we present here support the view that our approach produces the most conservative constraints on the parameter spaces of alternative dark matter models relative to the standard Λ CDM paradigm. Efforts such as these complement various observation-based analyses such as measurements of the X-ray spectra of dark matter-dominated systems, the Lyman α forest ([Iršič et al. 2024](#)), and gravitational lensing ([Enzi et al. 2021](#); [Zelko et al. 2022](#)).

4 DISCUSSION

The ν MSM is an appealing, physically motivated alternative to the Λ CDM paradigm. It provides a plausible explanation for the extremely small masses of the active neutrinos in the Standard Model of particle physics and introduces a mechanism to produce the matter–anti-matter asymmetry in the Universe. Through these processes it can produce a dark matter particle candidate in a plausible range of parameter space that appears to be consistent with astrophysical constraints. In certain parameterizations of the ν MSM the sterile neutrino dark matter behaves relativistically at early times and suppresses the formation of dark matter structure at and below the scale of dwarf galaxies. Such departures from the predictions of Λ CDM could manifest as a suppression of the number of low-mass satellite galaxies around Milky Way mass hosts. This provides a useful metric to evaluate the viability of different parameterizations of the model (this approach is described in detail in [Newton et al. 2021](#)). We exploit this to constrain the two-dimensional parameter space of the ν MSM.

The choices that are adopted to populate dark matter substructure with galaxies play a particularly important role in setting the stringency of the constraints. Scenarios in which the subhalo occupation fraction is high exclude less of the model parameter space because more parameterizations are consistent with the inferred total number of Milky Way satellite galaxies. We rule out a large fraction of the parameter space below $M_s = 7.1$ keV when assuming that all dark matter substructure hosts galaxies (see Fig. 2); an extreme as-

sumption that is likely to be physically unrealistic. The advantage of this choice is that the results provide robust lower limits that are independent of assumptions about the details of galaxy formation physics. The rest of the parameter space is largely unconstrained; in this regime the most compelling constraints come from observational analyses of X-ray non-detections, although these are subject to modelling uncertainty ([Horiuchi et al. 2014](#); [Neronov et al. 2016](#); [Ng et al. 2019](#); [Dessert et al. 2020b](#); [Roach et al. 2020](#); [Foster et al. 2021](#); [Roach et al. 2023](#)).

Adopting physically motivated galaxy formation prescriptions, as we do to obtain the results in Fig. 3, lowers the subhalo occupation fraction and rules out large swathes of parameter space below $M_s = 10$ keV, and all parameterizations at and below $M_s = 4$ keV. In both cases, our fiducial results suggest that Milky Way satellite counts alone are insufficient to exclude all parameterizations of the ν MSM with $M_s = 7.1$ keV, which is favoured as an explanation for the 3.55 keV excess detected in the X-ray spectra of some galaxies and clusters. In both scenarios, the shapes of the exclusion regions are affected by the non-monotonic evolution of the momentum distribution of the dark matter as a function of θ_e at fixed M_s . The coldest momentum distributions are typically found at the logarithmic midpoint between the dark matter under- and over-production bounds.

The constraints could be strengthened further if the mass of the Milky Way halo is lower than currently assumed. We determine our fiducial results by marginalizing over the uncertainties in the [Callingham et al. \(2019\)](#) estimate of $M_{200}^{\text{MW}} = 1.17^{+0.21}_{-0.15} \times 10^{12} M_\odot$. The closest recent comparable analysis to ours assumes $M_{200}^{\text{MW}} = 1.4 \times 10^{12} M_\odot$ ([Nadler et al. 2021](#)). A synthesis of the mass estimates spanning the past two decades favours $M_{200}^{\text{MW}} = 8.5 \times 10^{11} M_\odot$ ([Bird et al. 2022](#)), although this is 50 per cent more massive than the results derived from recent analyses using the extensive *Gaia* data set of six-dimensional phase space information about the Milky Way stellar halo. Computing our constraints using $M_{200}^{\text{MW}} = 0.5 \times 10^{12} M_\odot$ improves the stringency of our results, which is especially dramatic when we adopt the `GALFORM` prescription to populate the subhaloes with galaxies. In this case, we rule out all parameterizations of the ν MSM at and below $M_s = 14$ keV with at least 95 per cent confidence and strongly exclude ν MSM sterile neutrinos as the sole explanation for the 3.55 keV excess. The latter finding holds for nearly all parameterizations of reionization except in the late-finishing scenarios with $z_{\text{reion}} = 6$ and $V_{\text{cut}} = 25 \text{ km s}^{-1}$ (not shown). A recent analysis of the Lyman β forest suggests that reionization may finish as late as $z_{\text{reion}} = 5.5$ ([Zhu et al. 2022](#)). Our results (see Fig. 4) suggest that the $M_s = 7.1$ keV parameter space is unlikely to be fully closed by Milky Way satellite counts in this case; however, in combination with the lower limits from X-ray non-detections (also shown in Figs 2 and 3), this parameter space is strongly disfavoured.

The final important consideration folded into satellite count analyses such as ours is the estimated size of the total satellite galaxy population of the Milky Way. As we show in Appendix A and Fig. 5, this can affect the stringency of the constraints significantly. The true size of the Milky Way satellite galaxy population is unknown because most of the virial volume has not been surveyed. In recent years this figure has been updated several times in response to the influx of new data from several wide-area survey programmes and the application of different modelling techniques to account for incompleteness. Now, several estimates exist. When we adopt the value of $N_{\text{sat}}^{\text{MW}} = 183$ favoured by [Nadler et al. \(2020\)](#), which disagrees with our earlier estimate of $N_{\text{sat}}^{\text{MW}} = 124^{+40}_{-27}$ ([Newton et al. 2018](#)), we rule out all parameterizations at and below $M_s = 7.1$ keV using our fidu-

cial Milky Way mass and parameterization of reionization. This is significantly less restrictive than the constraints obtained by [Nadler et al. \(2021\)](#), who rule out all parameterizations of the ν MSM below $M_s = 17.5$ keV when assuming this number of satellite galaxies. We are unable to account for the discrepancy between our results and theirs by changing the number of satellite galaxies alone.

Several components of the respective analyses could contribute to a discrepancy of this magnitude: (i) the width of the $N_{\text{sat}}^{\text{MW}}$ uncertainty distribution, (ii) artificially disrupted subhaloes in simulations, (iii) the assumed mass of the Milky Way halo, and (iv) how the subhaloes are populated with galaxies. We now discuss and compare each of these in turn. [Newton et al. \(2021\)](#) demonstrated that the width of the distribution describing the uncertainty in the estimate of $N_{\text{sat}}^{\text{MW}}$ affects the stringency of the constraints, and that broader distributions can weaken them by as much as 15 per cent. We use the [Newton et al. \(2018\)](#) probability distribution to model this uncertainty, which is slightly broader than the one used by [Nadler et al. \(2021\)](#); however, the discrepancy is marginal so this is likely to be a subdominant effect.

[Newton et al. \(2021\)](#) also showed that the artificial disruption of low-mass subhaloes caused by limited numerical resolution affects the constraints. Failing to account for this population, some of which could in principle host galaxies, artificially strengthens the constraints in analyses of this type. [Nadler et al. \(2021\)](#) attempt to account for such artificially destroyed subhaloes, finding that they comprise only 10 per cent of the whole subhalo population in gravity only zoom-in simulations of Milky Way mass haloes with a particle mass resolution of $3 \times 10^5 h^{-1} M_{\odot}$ ([Mao et al. 2015](#)). This fraction is significantly less than the sevenfold increase in the number of subhaloes suggested by [Newton et al. \(2021\)](#), in particular see fig. 7) for similarly massive host haloes drawn from the COCO simulations, which have a comparable mass resolution. This discrepancy is a potentially significant factor in the disparity between our results and theirs. It also highlights the considerable uncertainty that remains about the proper treatment of prematurely destroyed subhaloes. For example, [Benson & Du \(2022\)](#) found that artificial disruption in the Caterpillar simulations reduces the host’s subhalo population by 10–20 per cent. Most of the destruction is concentrated in the centre of the host, where as much as half of the subhaloes are destroyed by numerical instability. These results are consistent with the estimates used above. A related issue concerns the modelling of the stellar component of prematurely destroyed subhaloes, which is poorly understood at present. It is unclear what fraction of the prematurely destroyed subhaloes would host an observable galaxy, and to what extent their stars would be affected by tidal stripping. It is thus an important systematic in satellite number count analyses.

We mentioned previously that the Milky Way halo mass adopted by [Nadler et al. \(2021\)](#) is 20 per cent larger than our fiducial assumption. As choosing a more massive Milky Way halo mass weakens their constraints slightly, we dismiss this as having only a negligible contribution to the discrepancy between the two sets of results. Finally, as we showed in Sections 3.1 and 3.2, the procedure used to populate dark matter subhaloes with galaxies affects the constraints. [Nadler et al. \(2021\)](#) use subhalo abundance matching to determine what fraction of the subhalo population hosts galaxies, whereas we adopt physically motivated semi-analytic prescriptions implemented in GALFORM.

Subhalo abundance matching in the relevant mass regime has been shown to be inconsistent with the results of high resolution simulations by [Sawala et al. \(2015\)](#). By contrast, GALFORM provides a more nuanced physical portrayal of the complexities of galaxy formation on small scales, in particular, processes such as star form-

ation and feedback; reionization; and gas heating and cooling; albeit with some simplifying assumptions. Although GALFORM is not calibrated to reproduce observational results at the scales of interest here, it nonetheless performs well when compared with observations of the abundance and radial profile of Milky Way satellite galaxies ([Bose et al. 2018, 2020](#)) as well as with high-resolution hydrodynamical simulations that self-consistently track the evolution of low-mass dark matter haloes and their baryonic components (e.g. [Grand et al. 2021](#)). In comparison, the abundance matching approach suppresses the formation of faint galaxies more aggressively than we find when applying GALFORM. When combined with the possible under-correction for prematurely destroyed subhaloes, stronger constraints are an inevitable outcome. We believe these two methodological differences are the root causes of the discrepancy between the results, although this can only be confirmed with a more detailed investigation and comparison. An analysis such as this is beyond the scope of this work and we leave it to other studies.

Our fiducial results alone do not exclude the ν MSM as an explanation for the 3.55 keV excess; however, they do significantly restrict the parameter space at $M_s = 7.1$ keV. While X-ray non-detections already suggest that the ν MSM cannot explain the 3.55 keV excess, the lower limits are affected by uncertainties in modelling astrophysical backgrounds that could weaken these conclusions. Further light will be shed on this question by *XRISM* in the coming months. The *Resolve* instrument onboard *XRISM* has sufficient resolution to determine what flux originates from any emission line at 3.55 keV compared to any background, and also enough resolution in principle to measure the width of such lines. If these observations rule out all explanations within the realm of known physics, two possibilities remain: the ν MSM sterile neutrino could account for only some fraction of the cosmic dark matter abundance, or new physics are required to explain its origin.

5 CONCLUSIONS

In this work we impose robust constraints on the parameter space of the ν MSM by comparing predictions for the number of low-mass galaxies hosted by Milky Way mass ν MSM haloes against recent estimates of the size of the Milky Way satellite galaxy population. Our results complement the updated constraints determined from X-ray non-detections, and using other astrophysical probes such as gravitational lensing, the Lyman α forest, and the modelling of gaps in stellar streams.

To determine our constraints we use the Extended Press–Schechter formalism to produce reasonable estimates of the total abundance of substructure in Milky Way mass haloes (see Fig. 1). We calibrate it to match gravity only simulations corrected to account for subhaloes artificially destroyed by numerical effects. This is important because omitting the prematurely destroyed subhaloes strengthens the constraints artificially ([Newton et al. 2021](#)). We adopt two distinct approaches to populate the subhaloes with galaxies. The first approach, in which we make no assumptions about galaxy formation physics and presume that all subhaloes host a galaxy (see Section 3.1), produces the least stringent but most robust constraints. This rules out, with at least 95 per cent confidence, all parameterizations of the ν MSM with $M_s \leq 1.2$ keV independently of the effective active–sterile neutrino mixing angle and the Milky Way halo mass (see Fig. 2). When adopting the [Callingham et al. \(2019\)](#) estimate of the Milky Way halo mass we exclude all parameterizations with $M_s \leq 1.4$ keV. These results are consistent with constraints derived from theoretical and observational analyses of the phase

space density of dark matter within Milky Way dwarf satellite galaxies (Boyarsky et al. 2009). In the latter case, the parameter space with $M_s = 7.1$ keV is partially constrained at small mixing angles. If, as has been suggested recently, the Milky Way halo mass is at the lower end of estimates, the constraints at this rest mass strengthen somewhat. In combination with the lower limits determined from X-ray non-detections, the parameter space at $M_s = 7.1$ keV closes completely in the albeit unlikely scenario in which the subhalo occupation fraction is extremely high. Adopting a more realistic estimate of the abundance of satellite galaxies in Milky Way mass haloes strengthens the constraints further.

The second approach, in which we apply the GALFORM semi-analytic model of galaxy formation, incorporates physically motivated prescriptions of baryonic processes that suppress the formation of galaxies. In our analysis this renders more parameterizations of the ν MSM incompatible with estimates of the Milky Way satellite count and tightens the constraint on the viable parameter space significantly. One of the most important physical processes affecting the formation and evolution of low-mass galaxies is the reionization of hydrogen at early times. Using GALFORM we explore how changing the redshift at which reionization finishes, z_{reion} , and the circular velocity threshold, V_{cut} , below which galaxy formation in dark matter haloes is suppressed, affects the results (see Section 3.2). Adopting a fiducial parameterization of reionization with $z_{\text{reion}} = 7$ and $V_{\text{cut}} = 30 \text{ km s}^{-1}$, we rule out with at least 95 per cent confidence all parameter combinations of the ν MSM with $M_s \leq 4$ keV independently of effective mixing angle and Milky Way halo mass (see Fig. 3). The rest of the possible parameter space closes almost completely, and only the parameterizations of the $M_s = 7.1$ keV ν MSM with $0.4 \leq \sin^2(2\theta_e) / 10^{-10} < 10$ remain viable. All parameterizations of the ν MSM with $M_s = 7.1$ keV are excluded if $M_{200}^{\text{MW}} \leq 8 \times 10^{11} M_{\odot}$. Consistent with previous work (Newton et al. 2021), we find that increasing z_{reion} and V_{cut} strengthens the constraints, and the converse also holds (see Fig. 4).

A key assumption in analyses such as ours is the size of the Milky Way satellite galaxy population, which is unknown because most of the virial volume has not been surveyed yet. Our fiducial analysis adopts the Newton et al. (2018) estimate of the total population; however, several larger estimates have been published since then. Assuming larger values of the Milky Way satellite count rules out larger fractions of the ν MSM parameter space and strengthens our constraints somewhat (see Fig. 5). Notably, if $N_{\text{sat}}^{\text{MW}} = 183$ we rule out all parameterizations of the ν MSM with $M_s \leq 7.1$ keV, thus excluding the ν MSM as the origin of the 3.55 keV excess. However, compared to recent literature our constraints are less stringent.

We are unable to reproduce the strongest constraints reported by Nadler et al. (2021) even when we adopt a significantly larger number of Milky Way satellites. We attribute the disparity between our results and theirs to both the different choice of particle physics calculation and to the differing methodologies used to populate the subhaloes with galaxies. The physically motivated semi-analytic prescription in GALFORM, which we use, contrasts with the subhalo abundance matching adopted in Nadler et al. (2021). The latter approach, which has been shown to be inconsistent with the results of high resolution simulations by Sawala et al. (2015), suppresses the formation of faint galaxies more aggressively than the GALFORM model. A detailed and systematic comparison of the methodologies used in both studies, while undoubtedly of significant interest, is beyond the scope of this work and we leave this for future studies.

The recent launch of the JAXA *XRISM* satellite (Terada et al. 2021), an almost like-for-like replacement of the ill-fated *Hitomi* mission, will considerably improve observational capabilities at soft

X-ray energies once commissioning is complete. With higher sensitivity and resolution compared with previous instruments, *XRISM* is poised to confirm or refute the suggestion that the 3.55 keV excess corresponds to a detectable X-ray line. This unconfirmed signal, which currently lacks a clear astrophysical origin, has motivated considerable theoretical and observational efforts to ascertain whether it may originate from the dark sector. A successful confirmation of the signal and subsequent measurements of its width in various astrophysical systems could provide crucial evidence of the nature of the dark matter (Lovell 2023). However, our results imply that it is unlikely to correspond to the sterile neutrino proposed in the ν MSM framework.

ACKNOWLEDGEMENTS

ON thanks Mariana Jaber for useful discussions. ON acknowledges support from the Polish National Science Centre under grant UMO-2020/39/B/ST9/03494. ARJ and CSF were supported by STFC grant ST/L00075X/1. CSF acknowledges support from the European Research Council (ERC) through Advanced Investigator grant DMIDAS (GA 786910). MRL, SC, and JCH are supported by STFC grants ST/T000244/1 and ST/X001075/1. This work used the DiRAC@Durham facility managed by the Institute for Computational Cosmology on behalf of the STFC DiRAC HPC Facility (www.dirac.ac.uk). The equipment was funded by BEIS capital funding via STFC capital grants ST/K00042X/1, ST/P002293/1, ST/R002371/1 and ST/S002502/1, Durham University, and STFC operations grant ST/R000832/1. DiRAC is part of the National e-Infrastructure.

Software: This research made use of ASTROPY (The Astropy Collaboration et al. 2013, 2018), MATPLOTLIB (Hunter 2007), NUMPY (van der Walt et al. 2011; Harris et al. 2020), PYTHON (Van Rossum & Drake 2009), and SCIPY (Jones et al. 2011; Virtanen et al. 2020). This research also made use of the NASA Astrophysics Data System (<http://adsabs.harvard.edu/>) and the arXiv e-print service (<http://arxiv.org/>). We thank their developers for maintaining them and making them freely available.

DATA AVAILABILITY

The data used in this work are available upon reasonable request to the corresponding author. A repository of reduced data and scripts to produce the figures in this manuscript will be made available on GitHub² and will be archived in Zenodo.

References

- ATLAS Collaboration et al., 2021a, *Phys. Rev. D*, 103, 112006
- ATLAS Collaboration et al., 2021b, *JHEP*, 2021, 226
- Aad G., et al., 2023, *Phys. Lett. B*, 842, 137963
- Aalbers J., et al., 2023, *PRL*, 131, 041002
- Abazajian K. N., 2020, arXiv e-prints
- Abazajian K. N., et al., 2012, preprint ([arXiv:1204.5379](https://arxiv.org/abs/1204.5379))
- Abe K., et al., 2023, *Phys. Rev. D*, 108, 083022
- Adhikari R., et al., 2017, *JCAP*, 2017, 025
- Agnes P., et al., 2023, *Phys. Rev. D*, 107, 063001
- Aharonian F. A., et al., 2017, *ApJL*, 837, L15
- Albert A., et al., 2017, *Phys. Lett. B*, 769, 249

² Supplementary materials: [Musical-Neutron/nuMSM_constraints](https://github.com/Musical-Neutron/nuMSM_constraints)

- An R., Gluscevic V., Calabrese E., Hill J. C., 2022, *JCAP*, 2022, 002
- Anderson M. E., Churazov E., Bregman J. N., 2015, *MNRAS*, 452, 3905
- Angulo R. E., Hahn O., Abel T., 2013, *MNRAS*, 434, 3337
- Aprile E., et al., 2023, *PRL*, 131, 041003
- Asaka T., Shaposhnikov M., 2005, *Phys. Lett. B*, 620, 17
- Asaka T., Blanchet S., Shaposhnikov M., 2005, *Phys. Lett. B*, 631, 151
- Barbieri R., Nanopoulos D. V., Morchio G., Strocchi F., 1980, *Phys. Lett. B*, 90, 91
- Bardeen J. M., Bond J. R., Kaiser N., Szalay A. S., 1986, *ApJ*, 304, 15
- Benson A. J., Du X., 2022, *MNRAS*, 517, 1398
- Benson A. J., et al., 2013, *MNRAS*, 428, 1774
- Benson A. J., Ludlow A., Cole S., 2019, *MNRAS*, 485, 5010
- Bird S. A., et al., 2022, *MNRAS*, 516, 731
- Bond J. R., Cole S., Efstathiou G., Kaiser N., 1991, *ApJ*, 379, 440
- Bose S., Hellwing W. A., Frenk C. S., Jenkins A., Lovell M. R., Helly J. C., Li B., 2016, *MNRAS*, 455, 318
- Bose S., Deason A. J., Frenk C. S., 2018, *ApJ*, 863, 123
- Bose S., Deason A. J., Belokurov V., Frenk C. S., 2020, *MNRAS*, 495, 743
- Bower R. G., 1991, *MNRAS*, 248, 332
- Boyarisky A., Ruchayskiy O., Iakubovskiy D., 2009, *JCAP*, 2009, 005
- Boyarisky A., Ruchayskiy O., Iakubovskiy D., Franse J., 2014, *PRL*, 113, L251301
- Boyarisky A., Franse J., Iakubovskiy D., Ruchayskiy O., 2015, *PRL*, 115, L161301
- Boyarisky A., Drewes M., Lasserre T., Mertens S., Ruchayskiy O., 2019, *Prog. Part. Nucl. Phys.*, 104, 1
- Boyarisky A., Malyshev D., Ruchayskiy O., Savchenko D., 2020, preprint ([arXiv:2004.06601](https://arxiv.org/abs/2004.06601))
- Boylan-Kolchin M., Springel V., White S. D. M., Jenkins A., 2010, *MNRAS*, 406, 896
- Bulbul E., Markevitch M., Foster A., Smith R. K., Loewenstein M., Randall S. W., 2014, *ApJ*, 789, 13
- Bulbul E., Markevitch M., Foster A., Miller E., Bautz M., Loewenstein M., Randall S. W., Smith R. K., 2016, *ApJ*, 831, 55
- CMS Collaboration A. T., et al., 2021, *JHEP*, 2021, 153
- CRESST Collaboration et al., 2019, *Phys. Rev. D*, 100, 102002
- Callingham T. M., et al., 2019, *MNRAS*, 484, 5453
- Canetti L., Drewes M., Shaposhnikov M., 2012, *New Journal of Physics*, 14, 095012
- Canetti L., Drewes M., Shaposhnikov M., 2013, *PRL*, 110, L061801
- Cappelluti N., et al., 2018, *ApJ*, 854, 179
- Cautun M., et al., 2020, *MNRAS*, 494, 4291
- Cole S., Aragón-Salamanca A., Frenk C. S., Navarro J. F., Zepf S. E., 1994, *MNRAS*, 271, 781
- Cole S., Lacey C. G., Baugh C. M., Frenk C. S., 2000, *MNRAS*, 319, 168
- DEAP Collaboration et al., 2019, *Phys. Rev. D*, 100, 022004
- Davis M., Efstathiou G., Frenk C. S., White S. D. M., 1985, *ApJ*, 292, 371
- Dekker A., Ando S., Correa C. A., Ng K. C. Y., 2022, *Phys. Rev. D*, 106, 123026
- Dessert C., Rodd N. L., Safdi B. R., 2020a, *Physics of the Dark Universe*, 30, 100656
- Dessert C., Rodd N. L., Safdi B. R., 2020b, *Science*, 367, 1465
- Dessert C., Ning O., Rodd N. L., Safdi B. R., 2024a, *PRL*, 132, 211002
- Dessert C., Foster J. W., Park Y., Safdi B. R., 2024b, *ApJ*, 964, 185
- Di Mauro M., Hou X., Eckner C., Zaharijas G., Charles E., 2019, *Phys. Rev. D*, 99, 123027
- Di Mauro M., Pérez-Romero J., Sánchez-Conde M. A., Fornengo N., 2023, *Phys. Rev. D*, 107, 083030
- Drlica-Wagner A., et al., 2020, *ApJ*, 893, 47
- Efstathiou G., Frenk C. S., White S. D. M., Davis M., 1988, *MNRAS*, 235, 715
- Enzi W., et al., 2021, *MNRAS*, 506, 5848
- Fattahi A., et al., 2016, *MNRAS*, 457, 844
- Foster J. W., Kongsore M., Dessert C., Park Y., Rodd N. L., Cranmer K., Safdi B. R., 2021, *PRL*, 127, 051101
- Franse J., et al., 2016, *ApJ*, 829, 124
- Fukugita M., Yanagida T., 1986, *Phys. Lett. B*, 174, 45
- Gell-Mann M., Ramond P., Slansky R., 1979, preprint ([arXiv:1306.4669](https://arxiv.org/abs/1306.4669))
- Ghiglieri J., Laine M., 2015, *JHEP*, 2015, 171
- Grand R. J. J., et al., 2021, *MNRAS*, 507, 4953
- Gu L., Kaastra J., Raassen A. J. J., Mullen P. D., Cumbee R. S., Lyons D., Stancil P. C., 2015, *A&A*, 584, L11
- H.E.S.S. Collaboration et al., 2018, *PRL*, 120, 201101
- Harris C. R., et al., 2020, *Nature*, 585, 357
- Hellwing W. A., Frenk C. S., Cautun M., Bose S., Helly J., Jenkins A., Sawala T., Cytoński M., 2016, *MNRAS*, 457, 3492
- Hofmann F., Wegg C., 2019, *A&A*, 625, L7
- Hofmann F., Sanders J. S., Nandra K., Clerc N., Gaspari M., 2016, *A&A*, 592, A112
- Horiuchi S., Humphrey P. J., Oñorbe J., Abazajian K. N., Kaplinghat M., Garrison-Kimmel S., 2014, *Phys. Rev. D*, 89, 025017
- Hunter J. D., 2007, *Comput. Sci. Eng.*, 9, 90
- Iakubovskiy D., Bulbul E., Foster A. R., Savchenko D., Sadova V., 2015, preprint ([arXiv:1508.05186](https://arxiv.org/abs/1508.05186))
- IceCube Collaboration et al., 2022, *Phys. Rev. D*, 105, 062004
- Iršič V., et al., 2024, *Phys. Rev. D*, 109, 043511
- Jenkins A., Frenk C. S., White S. D. M., Colberg J. M., Cole S., Evrard A. E., Couchman H. M. P., Yoshida N., 2001, *MNRAS*, 321, 372
- Jones E., Oliphant T., Peterson P., 2011, SciPy Open Source Scientific Tools for Python, www.scipy.org
- Kennedy R., Frenk C., Cole S., Benson A., 2014, *MNRAS*, 442, 2487
- Komatsu E., et al., 2011, *ApJS*, 192, 18
- Lacey C., Cole S., 1993, *MNRAS*, 262, 627
- Lacey C. G., et al., 2016, *MNRAS*, 462, 3854
- Laine M., Shaposhnikov M., 2008, *JCAP*, 2008, 031
- Leo M., Baugh C. M., Li B., Pascoli S., 2018, *JCAP*, 2018, 010
- Lewis A., Challinor A., Lasenby A., 2000, *ApJ*, 538, 473
- Lovell M. R., 2023, *MNRAS*, 524, 6345
- Lovell M. R., Frenk C. S., Eke V. R., Jenkins A., Gao L., Theuns T., 2014, *MNRAS*, 439, 300
- Lovell M. R., et al., 2016, *MNRAS*, 461, 60
- Lovell M. R., et al., 2017, *MNRAS*, 468, 4285
- Lovell M. R., et al., 2019a, *MNRAS*, 485, 4071
- Lovell M. R., Iakubovskiy D., Barnes D., Bose S., Frenk C. S., Theuns T., Hellwing W. A., 2019b, *ApJL*, 875, L24
- Mao Y.-Y., Williamson M., Wechsler R. H., 2015, *ApJ*, 810, 21
- McDaniel A., Ajello M., Karwin C. M., Di Mauro M., Drlica-Wagner A., Sánchez-Conde M. A., 2024, *Phys. Rev. D*, 109, 063024
- Mikheyev S. P., Smirnov A. Yu., 1985, *Yadernaya Fizika*, 42, 1441
- Minkowski P., 1977, *Phys. Lett. B*, 67, 421
- Mohapatra R. N., Senjanović G., 1980, *PRL*, 44, L912
- Murgia S., 2020, *Annu. Rev. Nucl. Part. Sci.*, 70, 455
- Nadler E. O., Mao Y.-Y., Green G. M., Wechsler R. H., 2019, *ApJ*, 873, 34
- Nadler E. O., et al., 2020, *ApJ*, 893, 48
- Nadler E. O., et al., 2021, *PRL*, 126, 091101
- Necib L., Lin T., 2022, *ApJ*, 926, 189
- Neronov A., Malyshev D., Eckert D., 2016, *Phys. Rev. D*, 94, 123504
- Newton O., Cautun M., 2018, MW Satellite LF: V1.0.0 Release, Zenodo, [doi:10.5281/zenodo.1205622](https://doi.org/10.5281/zenodo.1205622), <https://zenodo.org/record/1205622>
- Newton O., Cautun M., Jenkins A., Frenk C. S., Helly J. C., 2018, *MNRAS*, 479, 2853
- Newton O., et al., 2021, *JCAP*, 2021, 062
- Ng K. C. Y., Roach B. M., Perez K., Beacom J. F., Horiuchi S., Krivonos R., Wik D. R., 2019, *Phys. Rev. D*, 99, 083005
- PICO Collaboration et al., 2019, *Phys. Rev. D*, 100, 022001
- PandaX-4T Collaboration et al., 2021, *PRL*, 127, 261802
- Parkinson H., Cole S., Helly J., 2008, *MNRAS*, 383, 557
- Peebles P. J. E., 1982, *ApJL*, 263, L1
- Perez K., Ng K. C. Y., Beacom J. F., Hersch C., Horiuchi S., Krivonos R., 2017, *Phys. Rev. D*, 95, 123002
- Planck Collaboration et al., 2020, *A&A*, 641, A6
- Press W. H., Schechter P., 1974, *ApJ*, 187, 425
- Regis M., et al., 2021, *JCAP*, 2021, 046
- Riemer-Sørensen S., 2016, *A&A*, 590, A71

Roach B. M., Ng K. C. Y., Perez K., Beacom J. F., Horiuchi S., Krivonos R., Wik D. R., 2020, *Phys. Rev. D*, 101, 103011

Roach B. M., et al., 2023, *Phys. Rev. D*, 107, 023009

Roche C., Necib L., Lin T., Ou X., Nguyen T., 2024, preprint (arXiv:2402.00108)

Ruchayskiy O., et al., 2016, *MNRAS*, 460, 1390

Sabti N., Alvey J., Escudero M., Fairbairn M., Blas D., 2020, *JCAP*, 2020, 004

Sawala T., et al., 2015, *MNRAS*, 448, 2941

Sawala T., et al., 2016, *MNRAS*, 457, 1931

Schneider A., 2015, *MNRAS*, 451, 3117

Schneider A., 2016, *JCAP*, 2016, 059

Sekiya N., Yamasaki N. Y., Mitsuda K., 2016, *PASJ*, 68, S31

Shah C., Dobrodey S., Bernitt S., Steinbrügge R., López-Urrutia J. R. C., Gu L., Kaastra J., 2016, *ApJ*, 833, 52

Shaposhnikov M., 2008, *JHEP*, 2008, 008

Shi X., Fuller G. M., 1999, *PRL*, 82, L2832

Simha V., Cole S., 2017, *MNRAS*, 472, 1392

Sonbas E., Rangelov B., Kargaltsev O., Dhuga K. S., Hare J., Volkov I., 2016, *ApJ*, 821, 54

SuperCDMS Collaboration et al., 2015, *Phys. Rev. D*, 92, 072003

Tamura T., et al., 2019, *PASJ*, 71, 50

Tashiro M., et al., 2018, in *Space Telescopes and Instrumentation 2018: Ultraviolet to Gamma Ray*. International Society for Optics and Photonics, p. 1069922, doi:10.1117/12.2309455, <https://www.spiedigitallibrary.org/conference-proceedings-of-spie/10699/1069922/Concept-of-the-X-ray-Astronomy-Recovery-Mission/10.1117/12.2309455.short>

Terada Y., et al., 2021, *JATIS*, 7, 037001

The Astropy Collaboration et al., 2013, *A&A*, 558, A33

The Astropy Collaboration et al., 2018, *AJ*, 156, 123

The Super-Kamiokande Collaboration et al., 2020, *Phys. Rev. D*, 102, 072002

Tumasyan A., et al., 2022a, *Eur. Phys. J. C*, 82, 153

Tumasyan A., et al., 2022b, *JHEP*, 2022, 62

Tumasyan A., et al., 2023, *JHEP*, 2023, 228

Urban O., Werner N., Allen S. W., Simionescu A., Kaastra J. S., Strigari L. E., 2015, *MNRAS*, 451, 2447

Van Rossum G., Drake F. L., 2009, *Python 3 Reference Manual*. CreateSpace, Scotts Valley, CA

Venumadhav T., Cyr-Racine F.-Y., Abazajian K. N., Hirata C. M., 2016, *Phys. Rev. D*, 94, 043515

Viel M., Becker G. D., Bolton J. S., Haehnelt M. G., 2013, *Phys. Rev. D*, 88, 043502

Virtanen P., et al., 2020, *Nature Methods*, 17, 261

Wang J., White S. D. M., 2007, *MNRAS*, 380, 93

Wolfenstein L., 1978, *Phys. Rev. D*, 17, 2369

Yanagida T., 1980, *Prog. Theor. Phys.*, 64, 1103

Yin W., et al., 2024, preprint (arXiv:2402.07976)

Zelko I. A., Treu T., Abazajian K. N., Gilman D., Benson A. J., Birrer S., Nierenberg A. M., Kusenko A., 2022, *PRL*, 129, 191301

Zhou Y., Li X., Huang Y., Zhang H., 2023, *ApJ*, 946, 73

Zhu Y., et al., 2022, *ApJ*, 932, 76

van der Walt S., Colbert S. C., Varoquaux G., 2011, *Comput. Sci. Eng.*, 13, 22

APPENDIX A: DEPENDENCE OF STRUCTURE FORMATION CONSTRAINTS ON THE TOTAL NUMBER OF MILKY WAY SATELLITES

The constraints obtained via satellite number counts are sensitive to the size of the Milky Way satellite galaxy population adopted for the analysis. This has not been measured yet because current surveys do not have sufficient depth to survey the entire Milky Way virial volume, nor do they cover the entire sky. In Fig. A1, we present the constraints we obtain by comparing Extended Press–Schechter

predictions of the total abundance of substructure in Milky Way mass haloes with four different estimates of the size of the Milky Way satellite galaxy population, $N_{\text{sat}}^{\text{MW}}$ (Newton et al. 2018; Drlica-Wagner et al. 2020; Nadler et al. 2020). As in Section 3.1, we marginalize over the uncertainties in the Callingham et al. (2019) estimate of the Milky Way halo mass. Our constraints become more restrictive as the assumed size of the Milky Way satellite galaxy population increases because this requires the parameterizations of the ν MSM model to produce more substructure to remain viable. For completeness we also show our results when adopting $N_{\text{sat}}^{\text{MW}} = 270$ (dot-dashed line), which was reported by Drlica-Wagner et al. (2020) and was used in the analysis conducted by Dekker et al. (2022). Adopting this value of $N_{\text{sat}}^{\text{MW}}$ produces very stringent constraints on the parameter space; however, Nadler et al. (2020) noted that this estimate is inflated because the satellite distribution was assumed to be isotropic.

Alongside our constraints we plot the constraint envelope reported by Dekker et al. (2022), in which they use an Extended Press–Schechter framework and adopt the conservative assumption that all subhaloes host galaxies, as we did in Section 3.1. As noted above, their adopted value of $N_{\text{sat}}^{\text{MW}} = 270$ is now recognised to be too large; however, the overall approach is similar to ours so we would expect our constraints obtained when assuming the same value to be comparable with theirs. As Fig. A1 shows, our constraints are less restrictive, particularly where the effective mixing angle is large. Four aspects of their analysis contribute to their stronger constraints. First, their Extended Press–Schechter framework typically underestimates the number of subhaloes that survive until $z = 0$ by up to 40 per cent compared with the results of N -body simulations from Lovell et al. (2014). This discrepancy rises to 60 per cent in the cold dark matter model (Dekker et al. 2022, appendix C). In part, this may be because they calibrate their Extended Press–Schechter framework by adopting values of the density field filter function parameters from Schneider (2015). The simulations used in that work do not account for subhaloes that were prematurely destroyed by numerical effects. We showed in Newton et al. (2021) that underestimating the abundance of substructure by omitting the population of artificially destroyed subhaloes suppresses f_{ν} and can artificially strengthen constraints on the parameter space of WDM models.

Secondly, their calculation of f_{ν} does not account fully for sources of uncertainty. The scatter in the subhalo mass function is modelled using a Poisson distribution, which is narrower than the negative binomial distribution favoured by N -body cosmological simulations (Boylan-Kolchin et al. 2010). Additionally, they do not account for the uncertainty in the estimate of the total Milky Way satellite galaxy population. Underestimating or omitting one or both of these sources of uncertainty can produce constraints that are too strict (Newton et al. 2021, section 2.4).

Third, they assume a Milky Way halo mass, $M_{200}^{\text{MW}} = 10^{12} M_{\odot}$, which is 20 per cent less massive than the Callingham et al. (2019) estimate that we use. Adopting smaller values of M_{200}^{MW} can increase the stringency of the constraints on the parameter space; however, as we showed in Section 3.1, when assuming that all subhaloes are populated by galaxies the variation of the constraints as a function of M_{200}^{MW} is not significant. Therefore, we think that this is a subdominant contribution to the discrepancy between our results and those of Dekker et al. in Fig. A1.

Finally, in common with Nadler et al. (2021), Dekker et al. adopt the ν MSM momentum distributions computed by Venumadhav et al. (2016). They are warmer than the momentum distributions we use, which complicates the comparison of our results with theirs.

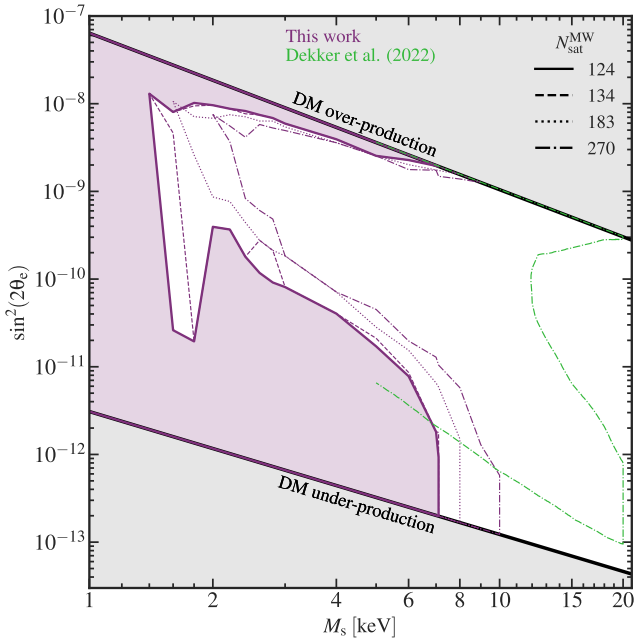


Figure A1. Structure formation constraints on the ν MSM parameter space from analyses of Milky Way satellite counts. As for several figures in the main text, the shaded regions in the upper and lower portions of the parameter space delimit parameter combinations for which the dark matter is over- or under-produced if resonantly produced sterile neutrinos compose all of the dark matter (Asaka et al. 2005; Schneider 2016). Our results are marginalized over the uncertainties in estimates of the Milky Way halo mass from Callingham et al. (2019). We compute constraint envelopes assuming a total Milky Way satellite galaxy population with a mean value of $N_{\text{sat}}^{\text{MW}} = 124$ (thick solid line), 134 (dashed line), 183 (dotted line), and 270 (dot-dashed line). Parameter combinations within the envelopes are ruled out with at least 95 per cent confidence. For comparison we show the constraint envelope from Dekker et al. (2022).

APPENDIX B: MODIFICATIONS TO THE MERGER TREE CONSTRUCTION ALGORITHM

In Newton et al. (2021, appendix B), we noted that the Monte Carlo merger trees generated in GALFORM using the standard implementation of the Parkinson et al. (2008) algorithm overestimate the abundance of low-mass galaxies by a factor of two. We addressed this by applying an empirical correction to the theoretical galaxy luminosity function in which the satellite galaxy absolute magnitude, M_V , predicted by GALFORM applied to the Monte Carlo merger trees is mapped to that predicted by GALFORM applied to the COCO simulation merger trees. This produced results in good agreement with the simulations; however, they are not self-consistent predictions of the Extended Press–Schechter methodology.

The discrepancy between the Monte Carlo and N -body predictions arises partly because the progenitor mass functions generated by the standard Parkinson et al. (2008) algorithm under-predict those produced in cosmological simulations at the low-mass end. This is because the Parkinson et al. (2008) algorithm was calibrated against the Millennium simulation, which cannot probe such low halo masses. The Parkinson et al. (2008) algorithm generates merger trees probabilistically via a sequence of branching events in which the mass, M_1 , in the halo at time, t_1 , may be partitioned into two lower-mass progenitors with masses, M_2 and $(M_1 - M_2)$, at an earlier time, t_2 . A complete merger tree is built up by repeating this process for each progenitor halo at each successive timestep. The size of the timestep, dt , is selected to be sufficiently small such that the halo is

unlikely to have more than two progenitors above some mass resolution threshold at the earlier time. The rate of progenitor formation is controlled by the binary merger branching rate,

$$\frac{dp}{d\omega} = \int_{M_{\text{min}}}^{M/2} \frac{M_1}{M'} \frac{df(M')}{dt} \frac{dS(M')}{dM'} \left| \frac{dt}{d\omega} \right| \times G[\omega, \sigma(M_1), \sigma(M')] dM', \quad (\text{B1})$$

where $\omega = \delta_{c,0}/D(t)$ is the ratio of the linear theory critical overdensity threshold for gravitational collapse in cold dark matter models, $\delta_{c,0}$, to the linear growth-rate factor, $D(t)$; M_{min} is the required minimum mass resolution of the merger tree; df/dt is the first-crossing rate distribution, the rate at which the excursion set trajectories first cross the overdensity threshold (Bond et al. 1991); $\sigma(M) = \sqrt{S(M)}$ is the square root of the variance, S , of the matter density field; and $G[\omega, \sigma(M), \sigma(M')]$ is an empirical modification introduced to obtain results consistent with those from cosmological cold dark matter simulations. In the standard implementation of the Parkinson et al. (2008) algorithm G is given by

$$G[\omega, \sigma(M_1), \sigma(M_2)] = G_0 \left[\frac{\sigma(M_2)}{\sigma(M_1)} \right]^{\gamma_1} \left[\frac{\omega}{\sigma(M_1)} \right]^{\gamma_2}, \quad (\text{B2})$$

which introduces the free parameters, G_0 , γ_1 , and γ_2 that are calibrated using dark matter-only cosmological simulations (see e.g. Benson et al. 2019, table 1).

As we discussed above, this implementation of the algorithm over-predicts the number of low-mass subhaloes because the empirical modification underestimates the simulated progenitor mass functions. We attempt to address this by introducing an explicit dependence on $D(t)$ and the logarithmic slope of the $\sigma(M)$ relation such that

$$G[\omega, \sigma(M_1), \sigma(M_2)] = G_0 \left[\frac{\sigma(M_2)}{\sigma(M_1)} \right]^{\gamma_1} \left[\frac{\omega}{\sigma(M_1)} \right]^{\gamma_2} \times \left\{ 1 - \left[\frac{\sigma(M_2)}{\sigma(M_1)} \right]^2 \right\}^{\gamma_3} D(t_2)^{\gamma_4} \left| \frac{d \ln \sigma(M_2)}{d \ln M} \right|^{\gamma_5}. \quad (\text{B3})$$

This parameterization was chosen to ensure that, if applied to a scale-free cosmology, the merger trees would satisfy the required self-similarity constraint (Efstathiou et al. 1988). This introduces a further three new free parameters: γ_3 , γ_4 , and γ_5 that are also determined via calibration to N -body simulations. Throughout this work, we use the latter form of G with $G_0 = 0.5024$, $\gamma_1 = 0.2493$, $\gamma_2 = -0.095846$, $\gamma_3 = 0.045166$, $\gamma_4 = 0.2342$, and $\gamma_5 = -0.1878$, based on a preliminary recalibration to recent simulations (A. J. Benson et al., in preparation).

This paper has been typeset from a $\text{\TeX}/\text{\LaTeX}$ file prepared by the author.